SERBIAN JOURNAL OF ELECTRICAL ENGINEERING
Vol. 11, No. 3, October 2014, 403-418

UDC: 537.852:616.831]:517.96 **DOI: 10.2298/SJEE140908029P**

The Electric Field Induced by Transcranial Magnetic Stimulation: A Comparison Between Analytic and FEM Solutions

Konstantin Porzig[1], Hartmut Brauer[1], Hannes Toepfer[1]

Abstract: The induced electric field profiles in a homogeneous isotropic sphere, were calculated and compared between an analytic and a finite-element method in the framework of transcranial magnetic stimulation (TMS). This model can also be applied for concentric spheres in the framework of magnetic induction tomography (MIT), non destructive testing (NDT) or to calculate the lead field in magnetoencephalography (MEG). The calculations were performed using Eaton's method as well as the finite-element program Comsol Multiphysics 4.2a (COMSOL Inc., Burlington, USA). A circular- and a figure-of-8 coil were used to operate as the sources of excitation. In our study the spherical volume conductor represents the human head consisting of grey matter. In order to quantify the differences between both methods an intense parameter study was performed. A comparison between both methods show a higher conformity than reported in previous studies. Regarding Eaton's method, the influence of the maximum order of approximation L and the number of elements per winding K was investigated. The maximum relative difference was approximately 0.3% for $L = 20$ and $K > 16$. Furthermore the relative efficiency of the algorithm was calculated to save computational time. With the presented results it is possible to use Eaton's method efficiently to compute the induced electric field profiles very quickly for example while searching for specific coil arrangements around the humans head, as in the case of deep brain transcranial magnetic stimulation (dTMS).

Keywords: Brain stimulation, Finite element method, Numerical analysis, Spherical volume conductor.

1 Introduction

Transcranial Magnetic Stimulation (TMS) is a procedure based on electromagnetic induction to excite nerves noninvasively and painlessly without the need of surgery. It was developed and first introduced at the University of Sheffield by Barker *et al.* in 1985 [1]. A transient current in an excitation coil

[1]Technische Universität Ilmenau, Department of Advanced Electromagnetics, Helmholtzplatz 2, 98393, Ilmenau, Germany;
E-mails: konstantin.porzig@tu-ilmenau.de; hartmut.brauer@tu-ilmenau.de; Hannes.toepfer@tu-ilmenau.de

creates a magnetic field which induces an electric field in the brain. This results in a temporary excitation or inhibitation of specific brain areas. The method is used in mapping studies to investigate the functional representations in the brain [2]. In the same way it is possible to test motor pathways by measuring the motor evoked potentials to evaluate neurological disturbances for example in patients with cervical spondylosis [3]. Furthermore it is known that a low frequency repetetive TMS (rTMS) at 1 Hz effectively reduces cortical activation to treat auditory phantom perceptions like chronic tinnitus or schizophrenia [4]. These examples demonstrate only a small area of application for magnetic stimulation. Therefore it is a main task to calculate the induced electric fields in the brain to ensure patient safety and to develop more efficient problem-specific excitation coils. In this paper Eaton's analytic formula [5] which is applicable to spherical volume conductors is compared to a finite-element method (FEM) using Comsol Multiphysics 4.2a [6]. This paper describes how an arbitrary coil geometry can be implemented in Eaton's formula by a simple numerical integration. The procedure is described for a circular- and a figure-of-8 coil with N windings. Furthermore a parameter study was performed to investigate the influence of the maximum order of approximation L and number of elements per winding K on the induced electric field profile. With this information it is possible to calculate a relative efficiency to provide values for L and K which yield an optimum between accuracy and computational expense.

2 Theory

To calculate the induced electric field in a spherical volume conductor, a brief review on electromagnetic theory is given in the following section. The complex electric field phasor $\boldsymbol{E}$ is given in the frequency domain by Faraday's law:

$$\nabla \times \boldsymbol{E} = -\mathrm{j}\omega \boldsymbol{B}\,. \tag{1}$$

The magnitude of the non-conservative electric field is directly proportional to the angular frequency ω and the magnetic flux density $\boldsymbol{B}$, which are determined from the current pulse in the excitation coil. The magnetic flux density $\boldsymbol{B}$ can be found from the curl of a vector potential $\boldsymbol{A}$:

$$\boldsymbol{B} = \nabla \times \boldsymbol{A}. \tag{2}$$

Substituting (2) into (1) and rearranging terms gives:

$$\nabla \times \left(\boldsymbol{E} + \mathrm{j}\omega \boldsymbol{A} \right) = \boldsymbol{0}. \tag{3}$$

This implies that the electric field $\boldsymbol{E}$ is given by:

$$\boldsymbol{E} = -\mathrm{j}\omega \boldsymbol{A} - \nabla\varphi\,, \tag{4}$$

where φ describes the scalar potential resulting from an accumulation of charge at the sphere boundary. The scalar potential φ satisfies Laplace's equation

$\Delta\varphi = 0$ inside the volume conductor [7]. Eaton solved (4) in spherical coordinates using spherical harmonic functions $Y_{lm}(\theta, \phi)$. The solution is valid as long as the frequency of excitation f is low enough to neglect propagation effects and skin depth δ_s [5]. To prove the assumptions made, the frequency of excitation as well as the material properties have to be considered. The frequency of the biphasic current pulse from a Magstim Rapid 2 stimulator (Magstim Company Ltd, Whitland, United Kingdom) was measured with a second coil and was found to be $f = 2.9$ kHz. The electrical conductivity $\sigma = 0.105$ S/m and relative permittivity $\varepsilon_r = 6.9 \cdot 10^4$ for grey matter (GM) were determined by the frequency of 2.9 kHz, using the Cole-Cole model from Gabriel et al. [8].

The skin depth δ_s is negligible if the following inequality is fulfilled:

$$\left(\frac{2R}{\delta_s}\right)^2 << 1, \tag{5}$$

where R is the radius of the human head. With the skin depth δ_s given by

$$\delta_s = \sqrt{\frac{2}{\omega\mu\sigma}}. \tag{6}$$

Then (5) becomes

$$2\omega\mu\sigma R^2 << 1. \tag{7}$$

With $R \approx 0.1$ m and a maximum frequency component of the transient current pulse of $f = 100$kHz the term on the left in (7) equals $1.6 \cdot 10^{-3}$. Therefore, skin depth is negligible even for a frequency of 100 kHz. To neglect propagation effects the location dependent phase shift factor $e^{(-jk|\boldsymbol{r}-\boldsymbol{r}'|)}$ has to be evaluated. The complex k is given in [9] and yields to:

$$k = \sqrt{\omega\mu\left(\omega\varepsilon - j\sigma\right)}. \tag{8}$$

Splitting k into real and imaginary parts gives:

$$\mathrm{Re}\{k\} = \sqrt{\frac{\omega\mu}{2}\left(\omega\varepsilon + \sqrt{\left(\omega\varepsilon\right)^2 + \sigma^2}\right)} \tag{9}$$

and

$$\mathrm{Im}\{k\} = -\sqrt{\frac{\omega\mu}{2}\left(-\omega\varepsilon + \sqrt{\left(\omega\varepsilon\right)^2 + \sigma^2}\right)}. \tag{10}$$

The imaginary part of k is a damping coefficient and the real part determines the phase shift in a certain distance from the source $|\boldsymbol{r}-\boldsymbol{r}'|$. Assuming a distance from the source of $|\boldsymbol{r}-\boldsymbol{r}'| = 2R$, which is an approximation of the diameter of the human head, the damping term in case of GM are shown in

Table 1. The phase shift of −2.78° at the opposite site of the head indicates, that propagation effects are negligible in the framework of TMS.

Table 1
Phase shift factor for GM ata maximum frequency of 100 kHz.

Damping term $e^{\mathrm{Im}\{k\}2R}$	Phase shift term $e^{-j\mathrm{Re}\{k\}2R}$	Phase $-\mathrm{Re}\{k\}R\frac{360°}{\pi}$
0.9586	$e^{-j0.0484}$	–2.78°

3 Methods

3.1 Model definition

The geometry used to model the human head is a spherical volume conductor with a radius of $R = 81$ mm which represents the layer of GM [10]. The sphere is centered at the origin of the coordinate system. The excitation coil is positioned 17 mm above the sphere in a height $h = 98$ mm considering the presence of cerebrospinal fluid, skull and scalp. These layers are not taken into account in this study. The coil current is modeled with a maximum rate of change of $\mathrm{d}i/\mathrm{d}t = 100$ A/µs at $t = 0$, which corresponds to a usual stimulator output at 100% [11]. This results in combination with a fundamental frequency of a biphasic TMS pulse of $f = 2.9$ kHz in a current amplitude of:

$$I = \frac{1}{\omega}\frac{\mathrm{d}i}{\mathrm{d}t}\Big|_{t=0} = 5488.1\,\mathrm{A}. \tag{11}$$

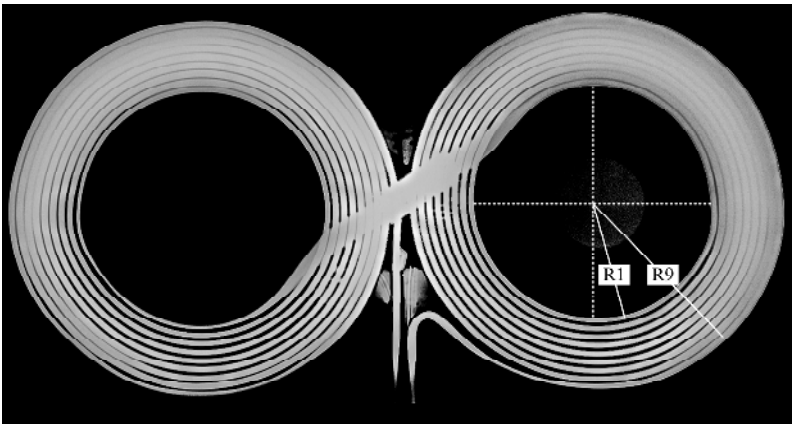

Fig. 1 – *X-ray picture of the* 2nd *Generation Double* 70 mm *Coil – Std.-3191-00* (*Magstim Company Ltd, Whitland, United Kingdom*).
Each wing consists of 9 *windings seperated by* $\Delta R = 2$ mm.

3.2 Analytic method

Eaton's formulas are used to calculate the induced electric fields analytically. This method can also be applied to calculate the induced current density inside concentric spheres due to absence of radial components of the induced electric field [5]. All calculations are performed using the software package Mathematica 7 (Wolfram Research Inc., Champaign, USA). To implement the method, a numerical integration of the current along its path inside the coil has to be performed. In Eaton's formulas this information is stored in the complex vector coefficients $\boldsymbol{C}_{\mathrm{lm}}$:

$$\boldsymbol{C}_{lm} = \int_{\mathrm{coil}} \frac{Y_{lm}^{*}(\theta',\phi')}{(2l+1)r'^{l+1}} \boldsymbol{dl}'. \tag{12}$$

The numeric integration has to be performed for the indices l and m up to an order $l = L$, where L describes the maximum order of approximation. The distance from the origin to the differential current element $\boldsymbol{dl}'$ is r'. $Y_{lm}^{*}(\theta',\phi')$ are the complex conjugate spherical harmonics for l and m at the sources' inclination θ' and azimuth ϕ' in spherical coordinates. Therefore, depending on L, the number of spherical harmonics and thus numeric integrations M, which have to be calculated in advance is given by:

$$M(L) = \sum_{l=0}^{L} (2l+1). \tag{13}$$

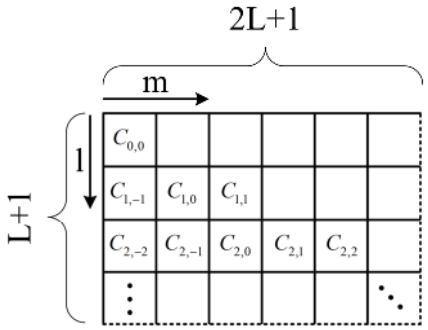

Fig. 2 – *Matrix of one component of the $\boldsymbol{C}_{l,m}$ coefficients. Each element contains the coefficient of the related spherical harmonic for l and m.*

It is mentioned that (12) has to be evaluated in Cartesian coordinates for further calculations. The goal of the numeric integration is to describe the integral in (12) as a discrete sum for a given coil geometry. Once the $\boldsymbol{C}_{\mathrm{lm}}$ coefficients are determined up to a given order of approximation L, they can be easily stored in a matrix and addressed by the indices l and m (Fig. 2). The implementation of the $\boldsymbol{C}_{\mathrm{lm}}$ coefficients into Eaton's equations is straightforward

and can be comprehended from [5]. The induced electric field $\boldsymbol{E}$ is calculated on a uniform grid inside the spherical volume conductor. The distance between the points was 2.5 mm in all directions, resulting in a total number of 72870 points inside the sphere.

3.2.1 Numerical integration of a circular coil with *N* windings

First, the numerical integration is described in the case of a simple circular coil. The coil lies in the *x*-*y* plane at a height *h* and its center coincides with the *z*-axis.

In the following, the number of turns is *N*, the turn index is *n* and the radius of the corresponding winding is R_n. The windings are defined to be concentric and each circle is divided into *K* elements with element index *k*. The variables $\theta'(n,k)$, $\phi'(n,k)$, $r'(n,k)$ and $\boldsymbol{dl'}(n,k)$ from (12) are calculated as a function of the winding index *n* and the element index *k*. Hence, by means of the principle of superposition, the complex vector coefficients $\boldsymbol{C}_\mathrm{lm}$ can be evaluated by adding up the contributions of all elements. All variables are calculated at the center of each element and kept constant inside. The approximated coefficients $\boldsymbol{C}_{lm}^{\approx}$ are converging for $K \to \infty$ against the analytic coefficients $\boldsymbol{C}_{lm}$.

In case of a circular coil, the distance $r'(n)$ and the polar angle $\theta'(n)$ of the current elements only depend on the winding index *n*.

$$r'(n) = \sqrt{R_n^2 + h^2}\,, \tag{14}$$

$$\theta'(n) = \arccos\left(\frac{h}{\sqrt{R_n^2 + h^2}}\right). \tag{15}$$

The azimuth $\phi'(k)$ only depends on the element index *k* and can be calculated by:

$$\phi'(k) = k\frac{2\pi}{K}\,. \tag{16}$$

Furthermore, the differential element $\mathbf{dl'}$ can be approximated by:

$$\mathbf{dl'}(n,k) \approx \frac{2\pi R_n}{K}\left[-\sin\left(k\frac{2\pi}{K}\right)\boldsymbol{e}_x + \cos\left(k\frac{2\pi}{K}\right)\boldsymbol{e}_y\right]. \tag{17}$$

Substituting (14 – 17) in (12) yields to the approximated complex vector coefficients $\boldsymbol{C}_{lm}^{\approx}$:

$$\begin{aligned}\boldsymbol{C}_{lm}^{\approx} = \sum_{n=1}^{N}\frac{2\pi R_n}{K(2l+1)\sqrt{R_n^2+h^2}^{\,l+1}}\cdot\sum_{k=0}^{K-1}Y_{lm}^{*}\left(\theta'(n),\phi'(k)\right)\cdot \\ \cdot\left(-\sin\left(k\frac{2\pi}{K}\right)\boldsymbol{e}_x + \cos\left(k\frac{2\pi}{K}\right)\boldsymbol{e}_y\right).\end{aligned} \tag{18}$$

The underlying symmetry simplifies the discretization procedure. No discretization error is made in terms of $r'(n)$ and $\theta'(n)$, due to the fact that the variables are constant for each turn. Therefore, it can be assumed that fewer elements K are needed to approximate the given coil geometry.

3.2.2 Numerical integration of a figure-of-8 coil with *N* windings

The numerical integration scheme of a figure-of-8 coil with N windings is based on the principle described in the previous section and is illustrated in Fig. 3. The coil lies in the x-y plane and is separated into a left and right part, each consisting of N concentric windings with radius R_n. Again, the principle of superposition was used to calculate the complex vector coefficients $\boldsymbol{C}_{lm}$, by summing up the contributions of all elements.

The distance $r'(n,k)$ is identical for the left and the right hand side of the coil and given by:

$$r'(n,k) = \sqrt{R_N^2 + R_n^2 - 2R_N R_n \cos\left(k\frac{2\pi}{K}\right) + h^2}, \tag{19}$$

where R_N is the radius of the largest winding.

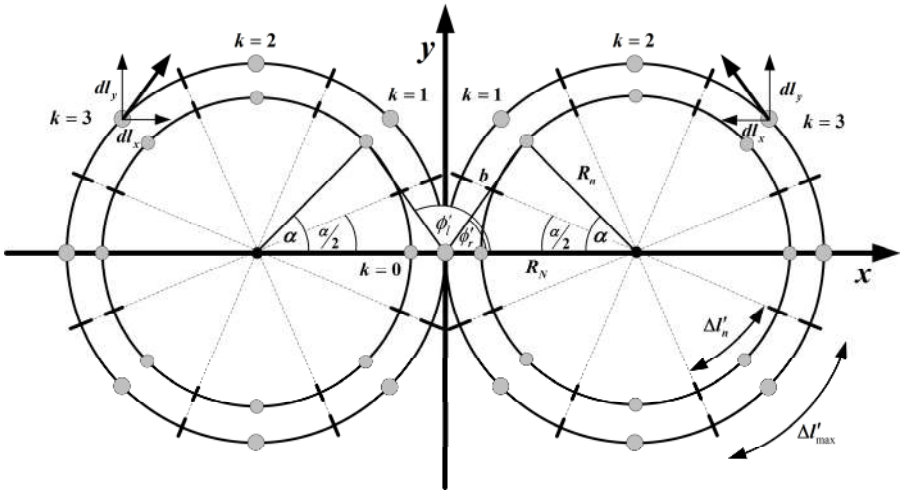

Fig. 3 – *Principle of discretization and numeric integration of a figure-of-8-coil with N windings* (*here: N* = 2, *K* = 8) *lying in the x-y plane at a height h.*

The polar angle $\theta'(n,k)$ is also identical for both sides:

$$\theta'(n,k) = \arccos\left(\frac{h}{r'(n,k)}\right). \tag{20}$$

In this case the variables $\phi'(n,k)$ and $\boldsymbol{dl}'(n,k)$ differ between the left and the right hand side of the figure-of-8 coil.

The azimuth $\phi_r'(n,k)$ for the right part of the coil, which lies in the first and fourth quadrant of the coordinate system, is different compared to the left part, which lies in the second and third quadrant. In consequence $\phi_r'(n,k)$ is given by:

$$\phi_r'(n,k) = \begin{cases} \arccos\left(G(n,k)\right) & \text{for } k\frac{2\pi}{K} \le \pi \\ -\arccos\left(G(n,k)\right) & \text{else} \end{cases} \tag{21}$$

with

$$G(n,k) = \frac{R_N^2 - R_N R_n \cos\left(k\frac{2\pi}{K}\right)}{R_N r'(n,k)}. \tag{22}$$

For the left hand side, the azimuth $\phi_l'(n,k)$ can be calculated by means of (21):

$$\phi_l'(n,k) = \pi - \phi_r'(n,k). \tag{23}$$

The differential elements $\boldsymbol{dl}_r'$ for the right and $\boldsymbol{dl}_l'$ for the left hand side, considering that the current is flowing in a counterclockwise and clockwise direction respectively, are given by:

$$\boldsymbol{dl}_r'(n,k) \approx \frac{2\pi R_n}{K}\left[-\sin\left(\pi - k\frac{2\pi}{K}\right)\boldsymbol{e}_x + \cos\left(\pi - k\frac{2\pi}{K}\right)\boldsymbol{e}_y\right], \tag{24}$$

$$\boldsymbol{dl}_l'(n,k) \approx \frac{2\pi R_n}{K}\left[\sin\left(k\frac{2\pi}{K}\right)\boldsymbol{e}_x - \cos\left(k\frac{2\pi}{K}\right)\boldsymbol{e}_y\right]. \tag{25}$$

Finally the approximated complex vector coefficients $\boldsymbol{C}_{lm}^{\approx}$ are given in (26) by substituting (19 – 25) in (12) and superimposing the left and the right side of the figure-of-8 coil.

The described integration scheme can also be used to model arbitrary coil geometries. At this point, the implementation of Eaton's method is straightforward and described in [5].

$$\begin{aligned} \boldsymbol{C}_{lm}^{\approx} = \sum_{n=1}^{N} \frac{2\pi R_n}{(2l+1)K}\Bigg[& \sum_{k=0}^{K-1} \frac{Y_{lm}^*\left(\theta'(n,k),\phi_r'(n,k)\right)}{r'(n,k)^{l+1}} \\ & \cdot\left(-\sin\left(\pi - k\frac{2\pi}{K}\right)\boldsymbol{e}_x + \cos\left(\pi - k\frac{2\pi}{K}\right)\boldsymbol{e}_y\right) + \\ + \sum_{k=0}^{K-1} & \frac{Y_{lm}^*\left(\theta'(n,k),\phi_l'(n,k)\right)}{r'(n,k)^{l+1}} \cdot\left(\sin\left(k\frac{2\pi}{K}\right)\boldsymbol{e}_x - \cos\left(k\frac{2\pi}{K}\right)\boldsymbol{e}_y\right)\Bigg]. \end{aligned} \tag{26}$$

3.3 Numerical FEM model

The software package Comsol Multiphysics 4.2a [6] is used to evaluate the induced electric fields numerically. In contrast to the analytic method, the FEM does not neglect the skin effect. Due to the given symmetry in geometry, the model can be reduced to one half with the boundary conditions $\boldsymbol{n}\times\boldsymbol{A} = \mathbf{0}$ and $\varphi = 0$ at the symmetry plane. The usage of infinite elements is prevented because of computational intensity. It has proved to be more efficient to enlarge the size of the outer boundary, where the boundary condition $\boldsymbol{n}\times\boldsymbol{A} = \mathbf{0}$ is defined. In order to be able to compare the solutions of both methods, the current inside the coil is modelled as line currents too. An appropriate fine mesh is generated, in order to ensure accurate results. The maximum size of the finite elements is 2 mm for the coil and the spheres surface, and 3 mm inside the sphere. The mesh used to perform the FEM calculations is shown in Fig. 4. It consists of 971.385 finite elements, resulting in 7.490.226 degrees of freedom to solve.

3.4 Error estimation and comparison of methods

Eaton's analytic method contains two interlaced approximations. One of them is the numeric integration of the coil current, where the number of elements per winding K influences the accuracy of the coil model. The second approximation is due to the use of spherical harmonics, where the maximum order L affects the result of the induced electric field $\boldsymbol{E}$. In order to investigate the influence of these two parameters, the solutions of the induced electric field are compared to the results of the FEM for different values of K and L. For the parameter study the more complicated figure-of-8 coil is used. The maximum number of elements per winding K is changing from 4 to 1024 and the maximum order of spherical harmonics L is varied from 1 to 30.

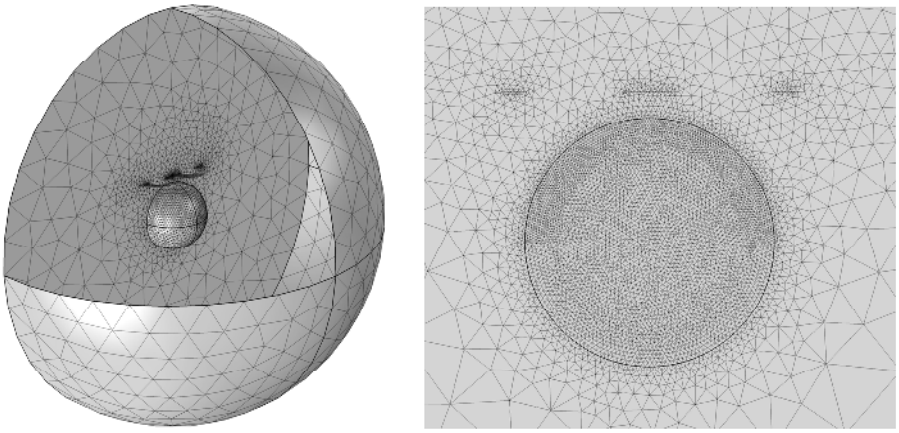

Fig. 4 – *Finite element mesh used in the numerical calculations with Comsol Multiphysics 4.2a.*

The normalized root mean square error δ in % is calculated for different K and L.

$$\delta = \frac{\sqrt{\frac{1}{N_o}\sum_{i=1}^{N_o}\left(E_i^{ana} - E_i^{fem}\right)^2}}{\max\left(E^{fem}\right) - \min\left(E^{fem}\right)} 100\% , \tag{27}$$

where E^{ana} and E^{fem} are the magnitudes of the induced electric field of Eaton's method and the FEM respectively, N_0 is the number of electric field values inside the sphere, defined by the uniform grid of the analytic method, and i is a point index. In addition, the maximum absolute difference $\Delta E_{\max}$ in V/m between both methods are computed in the given parameter space for K and L. In addition, the maximum relative difference $\Delta e_{\max}$ was calculated for values greater than 10% of the maximum value of E obtained with the FEM. Due to the fact that both parameters are affecting the computational expense, a relative efficiency ϵ was calculated to determine an optimal ratio between a given accuracy and computational cost. It is important to mention, that the numerical integration of the coil is a preprocessing step, where both parameters are affecting the computational expense. On the other hand the actual electric field calculation is only influenced by the maximum order of approximation L and the number of points N_0. For example, assuming a high number of points, resulting from a dense grid, the computational effort due to the numerical integration is small compared to the actual field computation. In order to take all these parameters into account, a cost factor γ was defined.

$$\gamma = \sqrt{KM\left(L\right) + N_0 M\left(L\right)} . \tag{28}$$

This factor is proportional to the number of mathematical operations needed to compute the induced electric field for a given coil discretization K, number of points N_0 and maximum order of approximation L, which is represented by the nonlinear function $M(L)$ from (13). The first term represents the computational effort due to the numerical integration and the second term represents the effort for the actual field computation. The relative efficiency ϵ is then calculated by:

$$\epsilon = \frac{1}{\delta\gamma}\frac{100\%}{\max\left(\delta\right)} . \tag{29}$$

4 Results

4.1 Field profiles

A 3-D plot of the induced electric field profiles, calculated with Comsol and Eaton's method for $K = 1024$ and $L = 30$ is given in Fig. 5. As expected, the maximum of the induced electric field is located under the center of the coil and

attenuates in greater depth. The results show a high conformity of both methods, if the parameters K and L are chosen sufficiently high. The plot of Comsol Multiphysics 4.2a shows the field profile at the surface, whereas the uniform grid used for Eaton's method results in a staircasing effect. In consequence, all points displayed for the analytic method lie inside the sphere and not at the boundary. Thus, the slightly different color scales and field maxima in Fig. 5 can be attributed to the different grids.

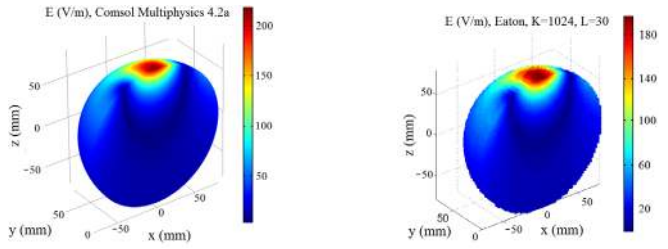

(a) (b)

Fig. 5 – *3-D surface plots of the induced electric field,* (a) *FEM (Comsol Multiphysics 4.2),* (b) *analytic method (Eaton).*

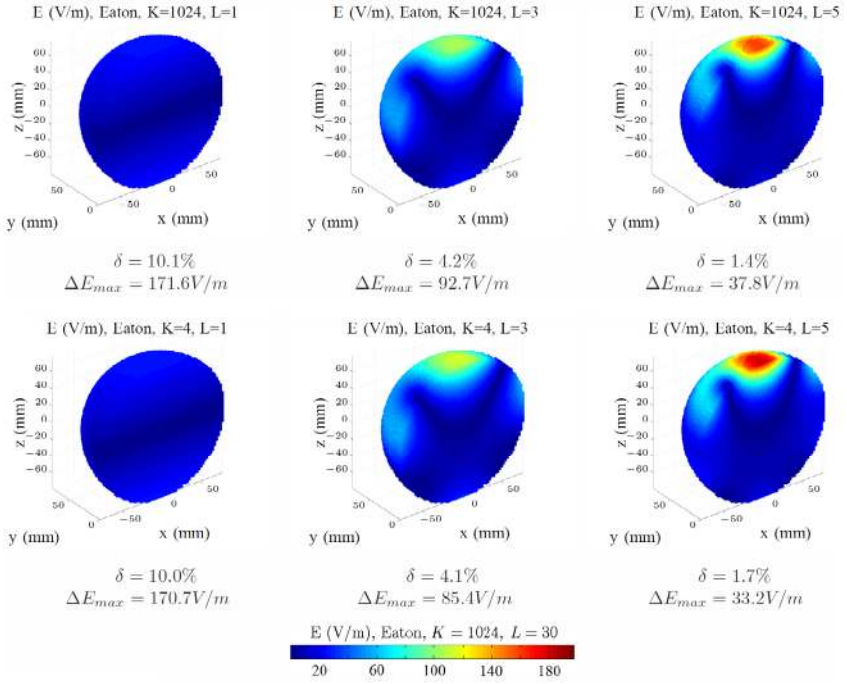

Fig. 6 – *Induced electric field profiles of the analytic method (Eaton) for different K and L. The colorbar corresponds to the analytic dataset with* $K = 1024$ *and* $L = 30$ *which was used as reference.*

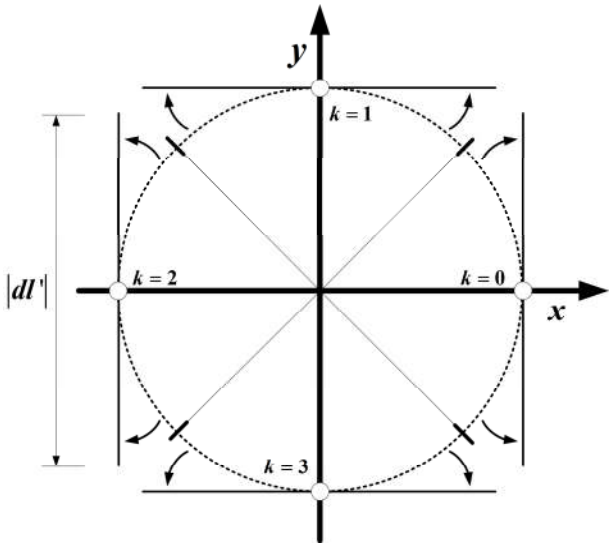

Fig. 7 – *Discretization principle of the numerical integration* ($K = 4$).

Several 3-D plots for different values of K and L are shown in Fig. 6. It was observed that the number of elements per winding K does not affect the field profile and the magnitude of the induced electric field as might expected. This can be explained by having a closer look at the discretization principle in Fig. 7. Even for low values of K such as 4, the most important parts of a winding are described and the formulas of the numerical integration ensure that the total length of all edges is independent of K. However, for high values of L, higher values of K should be used, due to an increased spatial variability of the spherical harmonics. Furthermore, Fig. 6 shows the evolution of the field profile for increasing order of magnitude L. A clear dependency of the magnitude of the induced electric field to the order of approximation L can be observed. In addition a fast convergence of the field profile is observed even for low values of L.

4.2 Error estimation

The normalized root mean square error δ and the maximum relative difference $\Delta e_{\max}$ are displayed in Fig. 8. The colormap is given in logarithmic scale to identify the differences more easily. Both, δ and $\Delta E_{\max}$ show similar characteristics which indicates that there are no regions inside the sphere, where the absolute difference increases unpredictably or has a different behaviour, compared to the mean error. As expected, both errors are increasing when K and L are decreased. However, the errors due to low values of K ($\delta \approx 0.2$–1.4%, $L > 5$) are about one magnitude lower compared to low values of L ($\delta \approx 1.4$–10%,

$K > 4$). The fast convergence of the errors for low values of $K = 4,...,10$ are confirming the reliability and robustness of the applied integration scheme. Our observations are in contrast to the investigation of Miranda *et al.*, where a maximum relative difference of 6.7% was reported for $L = 20$ [14]. The current study reveals a maximum relative difference of $\Delta e_{\max} \approx 0.3\%$ ($\delta = 0.005\%$, $\Delta E_{\max} = 0.25$V/m) for $L = 20$ and $K > 16$. All associated points, where the relative difference is maximum, were near the surface of the sphere as reported by Miranda *et al.* [14]. Therefore, our study shows that both methods are coinciding significantly better than reported earlier. Attention should be paid to the neglection of skin effect in Eaton's method. It has been demonstrated, that this assumption is reasonable in the framework of TMS due to the generally low conductivity of biological tissue together with the relative low frequency of excitation of 2-3 kHz. The simulation results of both methods confirm this.

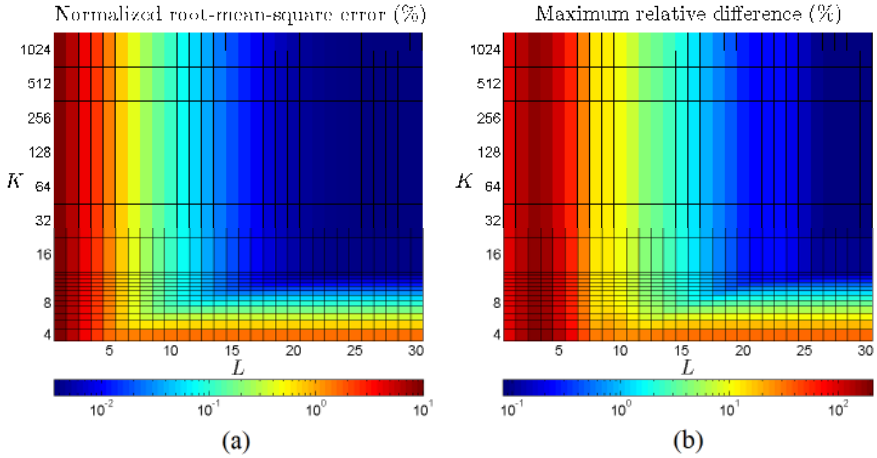

Fig. 8 – (a) *Normalized root-mean-square error* δ *and* (b) *Maximum relative difference* Δe_{max} *in dependence of the number of elements per winding K and maximum order of approximation L.*

4.3 Relative efficiency

The relative efficiency ϵ from (31) is calculated in the parameter space for K and L for different N_0. Fig. 9 shows the relative efficiency for two different numbers of grid points in the final computational grid $N_0 = 10$ and $N_0 = 1000$. In both cases a maximum of efficiency occurs at $L = 23$ and $K = 16$. Comparing both plots, it can be seen, that the relative efficiency ϵ becomes independent of K, when the number of points N_0 increases. This is a logical consequence and confirms the prediction in the previous section. Hence, if a fast approximation of the field profile due to a given coil configuration is needed with a relatively low amount of points N_0, an appropriate low value of $K = 16$ is sufficient to

calculate the electric field profile with a minimum number of mathematical operations and computational time.

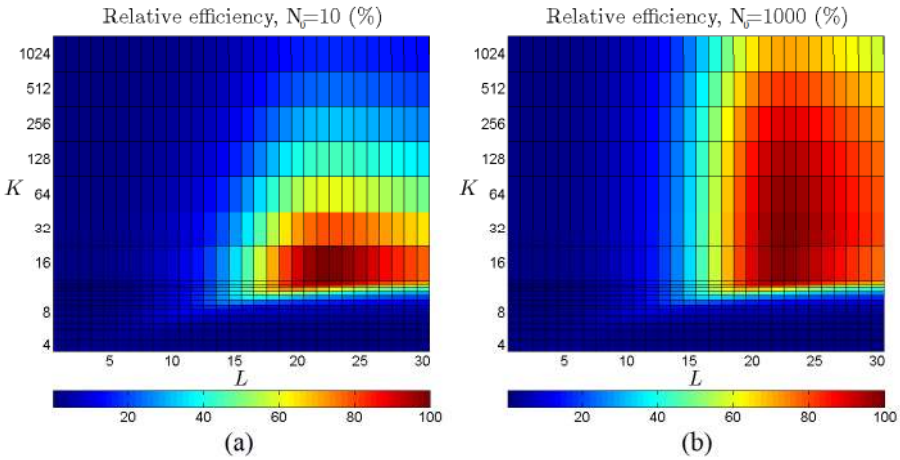

Fig. 9 – *Relative efficiency ϵ in dependence of the number of elements per winding K and maximum order of approximation L for* (a) $N_0 = 10$ *and* (b) $N_0 = 1000$ *points to calculate the induced electric field.*

5 Conclusion

This study describes the mathematical implementation of Eaton's method. Several parametrizable formulas for the numerical integration of currently available TMS coils, like a circular and a figure-of-8 coil are explicitly given. Furthermore X-ray images revealed the geometric properties of a Magstim - 2nd Generation Double 70mm Coil (Std.-3191-00). Our parameter study showed that Eaton's method is applicable to solve the given field problem with a much higher accuracy than previously reported by Miranda *et al.* [14]. The FEM is suitable to handle more complex geometries together with material properties like inhomogeneity [15] and anisotropy. However, the analytic approach together with the described and validated numeric integration scheme, described in this study, is helpful to estimate the induced electric field values for different coil geometries with significant lower computational cost. Especially in the framework of coil development for deep brain stimulation, a mesh independent, fast and efficient analytical approach is most helpful. Regarding this, Eaton's algorithm is analyzed with respect to accuracy and computational effort needed to calculate the induced electric fields, inside homogeneous or concentric spheres which have different electrical properties. Our study reveals a maximum efficiency, regarding accuracy and computational time, when using an maximum order of approximation of $L = 23$ and a number of elements per winding of $K = 16$. However, for a qualitative estimation of the induced electric

field profile, lower values of $L = 5,...,15$, depending on the number of coils around the volume conductor, can be used to reduce the number of mathematical operations and computation time.

Eaton's method can be used in other applications, such as magnetic induction tomography (MIT), nondestructive testing (NDT) or magneto encephalography (MEG), as long as skin effect is negligible.

Acknowledgement

We want to thank Sylvi Herzog most sincerly for numerious X-rays of our TMS coils and Lawrence Crowther together with Marek Ziolkowski for fruitful scientific discussions and all other people who supported us in our studies.

6 References

[1] A.T. Barker, R. Jalinous, I.L. Freeston: Non-invasive Magnetic Stimulation of Human Motor Cortex, Lancet, Vol. 325, No. 8437, May 1985, pp. 1106 – 1107.

[2] A. Pascual-Leone, N. Davey, J. Rothwell, E. Wasserman, B.K. Puri: Handbook of Transcranial Magnetic Stimulation, Arnold and Oxford University Press, NY, USA, 2002.

[3] M. Hallett: Transcranial Magnetic Stimulation and the Human Brain, Nature, Vol. 406, No. 6792, July 2000, pp. 147 – 150.

[4] B. Langguth, M. Zowe, M. Landgrebe, P. Sand, T. Kleinjung, H. Binder, G. Hajak, P. Eichhammer: Transcranial Magnetic Stimulation for the Treatment of Tinnitus: A New Coil Positioning Method and First Results, Brain Topography, Vol. 18, No. 4, Summer 2006, pp. 241 – 247.

[5] H. Eaton: Electric Field Induced in a Spherical Volume Conductor from Arbitrary Coils: Application to Magnetic Stimulation and MEG, Medical and Biological Engineering and Computing, Vol. 30, No. 4, July 1992, pp. 433 – 440.

[6] COMSOL Multiphysics Version 4.2a. COMSOL, Burlington, MA, USA, http://www.comsol.com/.

[7] J.D. Jackson: Classical Electrodynamics, John Wiley and Sons, NY, USA, 1999.

[8] S. Gabriel, R.W. Lau, C. Gabriel: The Dielectric Properties of Biological Tissues: III. Parametric Models for the Dielectric Spectrum of Tissues, Physics in Medicine and Biology, Vol. 41, No. 11, Nov. 1996, pp. 2271 – 2293.

[9] R. Plonsey, D.B. Heppner: Considerations of Quasi-stationarity in Electrophysiological Systems, Bulletin of Mathematical Biophysics, Vol. 29, No. 4, Dec. 1967, pp. 657 – 664.

[10] B.N. Cuffin, D. Cohen: Comparison of the Magnetoencephalogram and Electroencephalogram, Electroencephalography and Clinical Neurophysiology, Vol. 47, No. 2, Aug. 1979, pp. 132 – 146.

[11] R. Salvador, S. Silva, P.J. Basser, P.C. Miranda: Determining which Mechanisms Lead to Activation in the Motor Cortex: A Modeling Study of Transcranial Magnetic Stimulation using Realistic Stimulus Waveforms and Sulcal Geometry, Clinical Neurophysiology, Vol. 122, No. 4, Apr. 2011, pp. 748 – 758.

[12] A. Thielscher, T. Kammer: Linking Physics with Physiology in TMS: A Sphere Field Model to Determine the Cortical Stimulation Site in TMS, Neuroimage, Vol. 17, No. 3, Nov. 2002, pp. 1117 – 1130.

[13] A. Thielscher, T. Kammer: Electric Field Properties of Two Commercial Figure-8 Coils in TMS: Calculation of Focality and Efficiency, Clinical Neurophysiology, Vol. 115, No. 7, July 2004, pp. 1697 – 1708.

[14] P.C. Miranda, M. Hallett, P.J. Basser: The Electric Field Induced in the Brain by Magnetic Stimulation: A 3-D Finite-element Analysis of the Effect of Tissue Heterogeneity and Anisotropy, IEEE Transactions on Biomedical Engineering, Vol. 50, No. 9, Sept. 2003, pp. 1074 – 1085.

[15] B. Granula, K. Porzig, H. Toepfer, M. Gacanovic: A Comparison between an A-V and V Formulation in Transcranial Magnetic Stimulation, Comsol Conference, Rotterdam, Netherlands, 23 – 25 Oct. 2013, pp. 1 – 6.